Interplanetary shock data base

Denny M. Oliveira[1,2]*

[1]Goddard Planetary Heliophysics Institute, University of Maryland, Baltimore County, Baltimore, MD, United States, [2]Geospace Physics Laboratory, NASA Goddard Space Flight Center, Greenbelt, MD, United States

KEYWORDS

interplanetary shocks, data set, shock impact angle, solar cycle, shock parameters

1 Introduction

Interplanetary (IP) shocks are frequently observed in the solar wind (Burlaga, 1971; Stone and Tsurutani, 1985). Many levels of different kinds of geomagnetic activity may follow the impact of IP shocks on the Earth's magnetosphere. Such effects are seen everywhere in the magnetosphere-ionosphere system, including radiation belt dynamics, magnetic field in geosynchronous orbit, field-aligned currents, ionospheric disturbances, satellite orbital drag, ground magnetometers, geomagnetically induced currents (GICs), and others (e.g., Echer et al., 2005; Tsurutani et al., 2011; Khazanov, 2016; Oliveira and Ngwira, 2017; Oliveira and Zesta, 2019; Abda et al., 2020; Smith et al., 2020; Bhaskar et al., 2021). The study of IP shocks is important for space weather purposes because shock impacts occur more frequently than geomagnetic storms and correlate well with solar activity (Oh et al., 2007; Kilpua et al., 2015; Echer et al., 2023). Therefore, keeping an updated and accurate IP shock data base is of primary importance to the scientific community.

Many IP shock parameters control shock geoeffectiveness, such as shock speeds, Mach numbers, and compression ratios (Craven et al., 1986; Kabin, 2001; Goncharov et al., 2014). Additionally, the shock impact angle, the angle the shock normal vector performs with the Sun-Earth line, has been shown to be a significant factor that controls shock geoeffectiveness (Oliveira and Samsonov, 2018; Oliveira, 2023). Many works have demonstrated with simulations and observations that, in general, the more frontal and the faster the shock, the higher the subsequent geomagnetic activity observed from the geospace to the ground (e.g., Takeuchi et al., 2002; Guo et al., 2005; Wang et al., 2006; Oliveira and Raeder, 2014; Oliveira and Raeder, 2015; Samsonov et al., 2015; Oliveira et al., 2016; Selvakumaran et al., 2017; Oliveira et al., 2018; Baker, 2019; Rudd et al., 2019; Shi et al., 2019; Oliveira et al., 2020; Xu et al., 2020; Oliveira et al., 2021).

The main goal of this short report is to release an expanded version of an IP shock data base that was published before (Oliveira and Raeder, 2015; Oliveira et al., 2018). A major component of this new shock data base is a revision of the methodology used to calculate shock impact angles and speeds with respect to past versions of this list. Additionally, more shock and solar wind parameters before and after shock impacts and geomagnetic activity information were included in the list.

This article is organized as follows. Section 2 discusses the methodology used for the computation of shock properties, including the data used and shock normal calculation methods. A shock example is shown in Section 3. Section 4 presents the IP shock data base and its components. Finally, Section 5 brings a few suggestions for future usage of this shock list, with focus on the role of shock impact angles in controlling the subsequent shock geoeffectiveness.

2 Methods

2.1 Solar wind plasma and interplanetary magnetic field data

Properties and normal vector orientations of IP shocks are computed with the use of solar wind plasma and interplanetary magnetic field (IMF) data collected by solar wind monitors upstream of the Earth at the Lagrangian point L1. The time coverage of this shock list ranges from January 1995 to May 2023. Wind plasma data are collected by the Solar Wind Experiment instrument with resolution of 92 s (Ogilvie et al., 1995), and Wind magnetic field data are collected by the Magnetic Field Investigation instrument with resolution of 3 s (Lepping et al., 1995). ACE (Advanced Composition Explorer) collects solar wind data (resolution 64 s) with the Solar Wind Electron, Proton and Alpha Monitor instrument (McComas et al., 1998), and magnetic field data (resolution 16 s) with the MAG magnetometer instrument (Smith et al., 1998). All the data used for computations is represented in geocentric solar ecliptic (GSE) coordinates.

2.2 SuperMAG ground magnetometer and sunspot number data

Supporting geomagnetic index data are provided by the SuperMAG initiative (Gjerloev, 2009). SuperMAG computes geomagnetic indices using larger numbers of magnetometers in comparison to traditional IAGA (International Association of Geomagnetism and Aeronomy) indices (Davis and Sugiura, 1966; Rostoker, 1972). The SuperMAG ring current index, SMR, is explained by Newell and Gjerloev (2012), and the SuperMAG auroral indices SME, SMU, and SML are documented in Newell and Gjerloev (2011). SMU is the upper envelope index, SML is the lower envelope index, and SME = SMU—SML. All SuperMAG index data have resolution of 1 min.

Another supporting data set, with daily sunspot number observations, is provided by sunspot Index and Long-term Solar Observations, Royal Observatory of Belgium, Brussels (Clette and Lefèvre, 2016). The sunspot number data base used in this report has been corrected and recalibrated according to the methods explained by Clette and Lefèvre (2016).

2.3 Computations of shock impact angles and shock-related parameters

For the purpose of shock normal computations at 1 AU, shock fronts are assumed to be planar structures larger than the Earth's magnetospheric system (Russell et al., 1983; Russell, 2000). Then, IP shock normal vectors can be computed if data from at least one spacecraft is available (Russell et al., 1983; Aguilar-Rodriguez et al., 2010; Trotta et al., 2023). Generally, shocks driven by CMEs (coronal mass ejections) have their shock normals with small deviation with respect to the Sun-Earth line, whereas shocks driven by CIRs (corotating interacting regions) have their shock normals with large deviations from the Sun-Earth line (Kilpua et al., 2015; Oliveira and

Samsonov, 2018). Such shock inclinations occur because CMEs tend to travel radially in the solar wind, while CIRs tend to follow the Parker spiral when slow speed streams are compressed by fast speed streams (Pizzo, 1991; Tsurutani et al., 2006; Cameron et al., 2019). An animation showing the different inclinations of a CME-driven shock and a CIR-driven shock can be accessed here: https://dennyo liveira.weebly.com/phd.html.

There are three different ways commonly used to compute shock normal orientations. They use magnetic field data only, solar wind velocity data only, and a combination of magnetic field and solar wind velocity data. Such methods are, respectively, named magnetic coplanarity (MC, Colburn and Sonett, 1966), velocity coplanarity (VC, Abraham-Shrauner, 1972), and three mixed data methods (MX1, MX2, MX3, Schwartz, 1998). The equations used are listed below.

$$\vec{n}_{MC} = \pm \frac{\left(\vec{B}_2 \times \vec{B}_1\right) \times \left(\vec{B}_2 - \vec{B}_1\right)}{\left|\left(\vec{B}_2 \times \vec{B}_1\right) \times \left(\vec{B}_2 - \vec{B}_1\right)\right|} \tag{1}$$

$$\vec{n}_{MX1} = \pm \frac{\vec{B}_1 \times \left(\vec{V}_2 - \vec{V}_1\right) \times \left(\vec{B}_2 - \vec{B}_1\right)}{\left|\vec{B}_1 \times \left(\vec{V}_2 - \vec{V}_1\right) \times \left(\vec{B}_2 - \vec{B}_1\right)\right|} \tag{2}$$

$$\vec{n}_{MX2} = \pm \frac{\vec{B}_2 \times \left(\vec{V}_2 - \vec{V}_1\right) \times \left(\vec{B}_2 - \vec{B}_1\right)}{\left|\vec{B}_2 \times \left(\vec{V}_2 - \vec{V}_1\right) \times \left(\vec{B}_2 - \vec{B}_1\right)\right|} \tag{3}$$

$$\vec{n}_{MX3} = \pm \frac{\left(\vec{B}_2 - \vec{B}_1\right) \times \left(\vec{V}_2 - \vec{V}_1\right) \times \left(\vec{B}_2 - \vec{B}_1\right)}{\left|\left(\vec{B}_2 - \vec{B}_1\right) \times \left(\vec{V}_2 - \vec{V}_1\right) \times \left(\vec{B}_2 - \vec{B}_1\right)\right|} \tag{4}$$

$$\vec{n}_{VC} = \pm \frac{\vec{V}_2 - \vec{V}_1}{\left|\vec{V}_2 - \vec{V}_1\right|} \tag{5}$$

In these equations, $\vec{B}$ is the magnetic field vector, and $\vec{V}$ is the solar wind velocity vector. Indices 1 and 2 represent the upstream (non-shocked) region, and downstream (shocked) region, behind of and ahead the shock, respectively. The sign of each vector $\vec{n}$ is arbitrary and can be chosen to indicate whether the normal vector points toward the downstream direction (+) or upstream direction (−) (Schwartz, 1998).

Eqs 1–5 provide a three-dimensional normal vector $\vec{n} = (n_x, n_y, n_z)$ in Cartesian coordinates, from which three angles can be extracted.

$$\theta_{x_n} = \cos^{-1}(n_x), \tag{6}$$

$$\varphi_{y_n} = \tan^{-1}\left(\frac{n_z}{n_y}\right), \tag{7}$$

$$\theta_{B_n} = \frac{\vec{n} \cdot \vec{B}_1}{|\vec{B}_1|}, \tag{8}$$

where θ_{x_n} is named the shock impact angle, the angle the shock normal vector performs with the Sun-Earth line, φ_{y_n} is the shock clock angle in the yz plane perpendicular to the Sun-Earth line (both angles in the satellite or Earth reference frame), and θ_{B_n} is the angle between the upstream magnetic field vector and the shock normal vector (in the shock reference frame).

Since the plasma mass flux must be conserved along the shock normal, $\rho_1 u_{n1} = \rho_2 u_{n2}$, with $u_{n1,n2} = v_s - \vec{V}_{1,2} \cdot \vec{n}$, the shock speed is computed as follows:

$$v_s = \vec{n} \cdot \left(\frac{\vec{V}_2 \rho_2 - \vec{V}_1 \rho_1}{\rho_2 - \rho_1}\right) \tag{9}$$

Other useful shock velocities are represented by.

$$c_s = \sqrt{\frac{\gamma P_1}{\rho_1}} \quad \text{sound speed,} \tag{10}$$

$$v_A = \frac{|\vec{B}_1|}{\sqrt{\mu_0 \rho_1}} \quad \text{Alfvén speed,} \tag{11}$$

$$v_{ms} = \frac{1}{2}\sqrt{v_A^2 + c_s^2 \pm \sqrt{(v_A^2 + c_s^2)^2 - 4v_A^2 c_s^2 \cos^2(\theta_{B_n})}}$$
$$\text{magnetosonic speed,} \tag{12}$$

where $\gamma = 5/3$ is the ratio of the solar wind heat capacity with constant pressure to the heat capacity with constant volume; P_1 is the upstream solar wind thermal pressure; ρ_1 is the upstream solar wind density; and $\mu_0 = 4\pi \times 10^{-7}$ N/A^2 is the magnetic vacuum permeability. The positive solution of Eq. 12 gives the fast magnetosonic speed, whereas the negative solution yields the slow magnetosonic speed (Jeffrey and Taniuti, 1964; Priest, 1981; Boyd and Sanderson, 2003).

Shock strengths are usually represented by specific Mach numbers. With $u = v_s - \vec{V} \cdot \vec{n}$ being the relative speed between the shock speed and the local solar wind velocity, the Mach numbers are represented by.

$$M_A = \frac{u}{v_A} \quad \text{Alfvénic Mach number,} \tag{13}$$

$$M_s = \frac{u}{v_{ms}^f} \quad \text{fast magnetosonic Mach number,} \tag{14}$$

where v_{ms}^f is the fast magnetosonic speed.

Finally, the strength of IP shocks can also be indicated by upstream and downstream solar wind plasma parameters and IMF. Such compression ratios are represented by.

$$X_n = \frac{n_2}{n_1} \quad \text{plasma number density compression ratio,} \tag{15}$$

$$X_{dp} = \frac{\rho_2 V_2^2}{\rho_1 V_1^2} \quad \text{dynamic pressure compression ratio,} \tag{16}$$

$$X_B = \frac{|\vec{B}_2|}{|\vec{B}_1|} \quad \text{magnetic field compression ratio.} \tag{17}$$

3 The IP shock of 23 June 2000 as an example

Figure 1, first published by Oliveira and Raeder (2015), shows an IP shock event that occurred on 23 June 2000 observed by ACE at 1226 UT upstream of the Earth at (x, y, z) = (239.9, 36.7, −0.7) R_E, where R_E is the Earth's radius = 6,371.1 km. Solar wind plasma and IMF data are depicted in the figure, along with SuperMAG geomagnetic index data. From top to bottom, the plot shows three components of the IMF (a); IMF magnitude (b); x component of solar wind velocity (c); y and z components of solar wind velocity (d); solar wind velocity magnitude (e); solar wind particle number density (f); solar wind dynamic pressure $P_{dyn} = \rho V^2$ (g); solar wind thermal temperature (h); SMR index (i); and SMU/SML indices (j). The vertical dashed magenta lines indicate the time of shock impact on the magnetosphere. The data were shifted to the magnetopause nose to match shock observations with the onsets in the ground

geomagnetic indices. The highlighted grey areas correspond to the shock upstream region (left) 10 to 5 min before shock impact, and shock downstream region (right), 5 to 10 min after shock impact. Average values of these regions are used in Eqs 1–5 for the computation of the shock normal orientations with the five different methods. Most shocks have the time windows mentioned above, but a few events have different time windows.

As discussed by Balogh et al. (1995) and Trotta et al. (2022), the length of the upstream and downstream windows around the shocks is an important factor in determining shock parameters. For example, Trotta et al. (2022) suggested a method to use windows with different lengths with short-length windows being located near the shock. This methodology provides statistical significance (including uncertainties) to the calculated shock parameters and reliability to the subsequent results. This approach will be applied to this shock list in a future work for further improvements of this shock data base.

The data shown in the figure is processed before plotting and before computing shock parameters and normal orientations. First, bad data points, such as 1E + 31 are replaced by nan ("not a number") values and subsequently linearly interpolated. Then, solar wind parameter data are interpolated, and IMF data are averaged to a uniform time cadence of 30 s. Differences between the non-interpolated and interpolated data are very small or nearly nonexistent around the shock onset. This process allows the time resolutions of both data sets to match to further perform computations that involve both data sets. The same technique was applied to all events in the shock data base.

Positive step-like enhancements are seen in all solar wind plasma parameters and IMF. This is a clear signature of a fast forward IP shock (Priest, 1981; Tsurutani et al., 2011; Oliveira, 2017). More information on the analysis of this event including shock normal orientations will be provided in the next section.

4 The IP shock data base

Previous versions of this current shock data base were published by Oliveira and Raeder (2015) and Oliveira et al. (2018). A few sources were used to compile these previous shock lists: a shock catalog provided by the Harvard-Smithsonian Center for Astrophysics and compiled by Dr. J. C. Kasper for Wind (http://www.cfa.harvard.edu/shocks/wi_data/) and ACE (http://www.cfa.harvard.edu/shocks/ac_master_data/); a shock list compiled by the ACE team (at http://www-ssg.sr.unh.edu/mag/ace/ACElists/obs_list.html#shocks); and another list published by Wang et al. (2010) with events from February 1998 to August 2008. New events were added by scanning solar wind and IMF data to detect shock events that satisfy the framework discussed in Section 2.3.

The IP shock data base consists of three files: 1) `full_shock_list_2023.txt`, a text file with 603 events; 2) `full_shock_params.cdf`, a cdf file with detailed information about each specific shock event; and 3) `read_shock.py`, a file that contains a short python routine to read information about a specific shock event. The SpacePy package (https://spacepy.github.io, Morley et al., 2011; Larsen et al., 2022) is required to extract shock information from the cdf file using `read_shock.py`, which is shown in Listing 1.
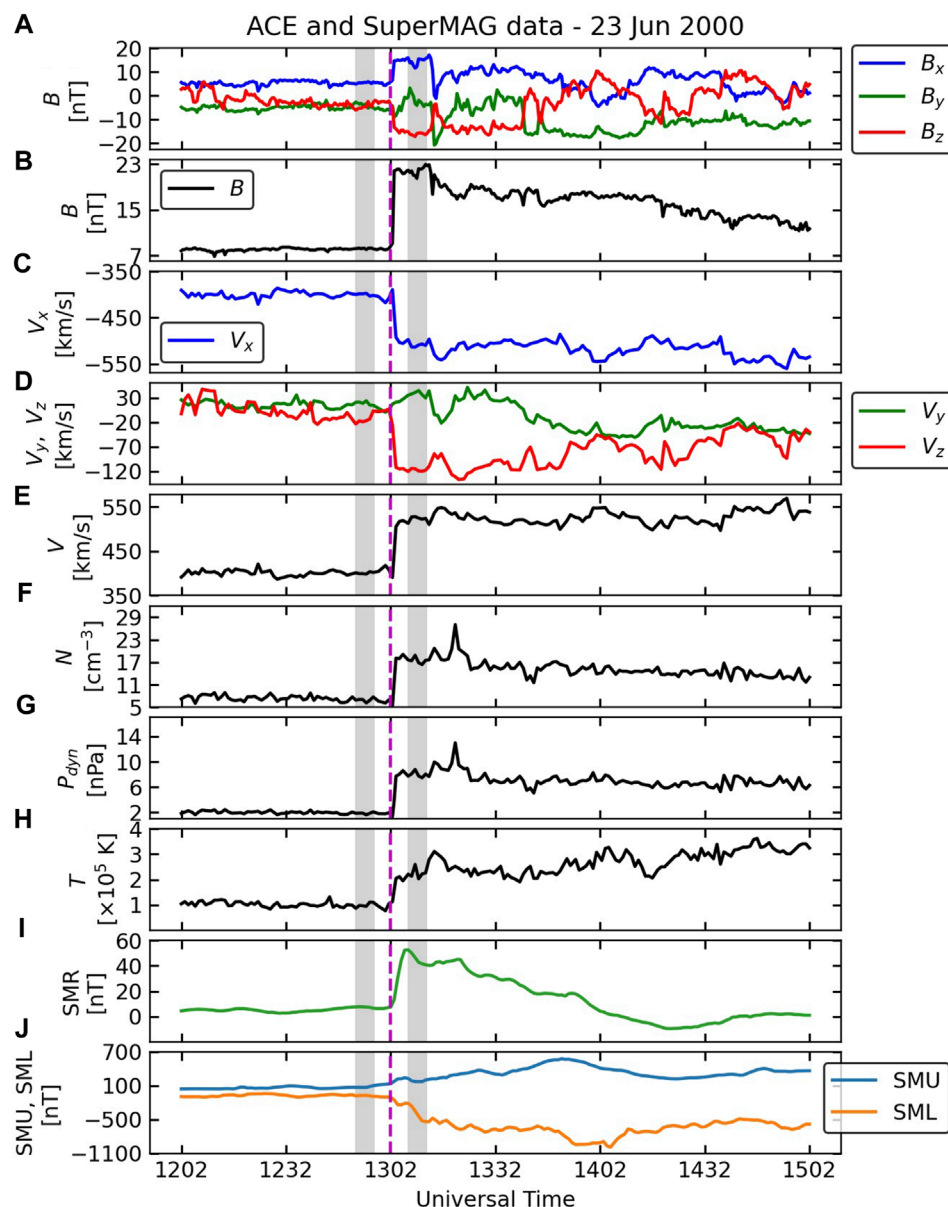
FIGURE 1
Interplanetary shock observed by ACE on 23 June 2000 and the subsequent geomagnetic activity represented by SuperMAG data. **(A)** three components of the IMF; **(B)** IMF magnitude; **(C)** x component of solar wind velocity; **(D)** y and z components of solar wind velocity; **(E)** solar wind velocity magnitude; **(F)** solar wind particle number density; **(G)** solar wind ram pressure; **(H)** solar wind thermal plasma density; **(I)** SMR index; and **(J)** SMU and SML indices.

```python
from spacepy import pycdf

def read_shock_cdf(sn):

    cdf = pycdf.CDF('full_shock_params.cdf')
    shock = cdf['SHOCK']

    for i in range(len(shock)):
        if (sn - 1) * 27 <= i <= (sn - 1) * 27 + 26:
            print(shock[i], end = '')
```

Listing 1. Python routine to extract information related to a specific shock event from the cdf file.

The input variable for the above routine is the shock number sn. The IP shock represented in Figure 1 is the event number 142 in the shock list. Therefore, read_shock.py can be run as shown in Listing 2.

The results for each shock are used to compose the shock list in the full_shock_list_2023.txt file. The file brings a header with the names of the variables (Table 1). The list also includes the position (in R_E) of the solar wind monitor (either Wind or ACE) whose data are used in the calculations, along with minimum SMR

values occurring in a time window of 2 hours after shock impact. This time window was chosen because amplitudes of geomagnetic activity response usually occur ~60 min after energy being released by the magnetotail (Bargatze et al., 1985; Oliveira and Raeder, 2015; Oliveira et al., 2021). Such values can be used in studies that aim to use shock observations during non-storm times.

Below are the steps taken to include a specific solution for each shock in the `full_shock_list_2023.txt` list. These are the major revisions made to the list in comparison to its previous versions.

1 A filter is passed on the data to replace bad data points (e.g., 1E+31) by nan values which are then replaced by interpolated/averaged values to a common time cadence for both data sets (IMF and solar wind parameter data).
2 The satellite (Wind or ACE) must be in the solar wind upstream of the Earth (x > 14 R_E).
3 If data of both satellites are simultaneously available, the data set with data of superior quality is used for computations.
4 Events with either M_A or M_s (or both) smaller than one are generally discarded. Events with such conditions are only included in the list if they trigger significant geomagnetic activity, such as SMR variations of at least 15 nT.
5 The solution obtained from Eqs 1–5 closest to the median value is selected to be included in the list. If the difference between the maximum and minimum values of θ_{x_n} is larger than 30°, the solution chosen for the list will be the one that shows more agreement with ground geomagnetic response, represented by the SuperMAG indices (SMR, SMU, SML, SME), as shown in previous publications (e.g., Wang et al., 2006; Oliveira and Raeder, 2015; Rudd et al., 2019; Oliveira et al., 2021).

The list version published by Oliveira and Raeder (2015) had 461 events, whereas the list published by Oliveira et al. (2018) had 547 events. This current data base has more events (603) and has a number of additional solar wind parameters and shock properties, which are shown in Table 1. The list time span, January 1995 to May 2023, includes two entire solar cycles (SC23 and SC24), the end of declining phase of SC22, and the beginning of ascending phase of SC25. Therefore, this data base provides a solid number of events for future statistical studies given an appropriate availability of data sets to be investigated.

Figure 2 represents general statistical features of the 603 events in the shock data base. Panel a shows yearly shock number

```
>>> from read_shock import read_shock_cdf
>>> read_shock_cdf(142)
---------------------------------------------------------------------------------------
 sn     date     UTS  UTM
 142 2000 06 23 1226  1302


 Spacecraft (sat): ac
 Position: X = 239.9 Re; Y =  36.7 Re; Z =  -0.7 Re


 Time windows
 Upstream:    5 to 10 minutes before shock
 Downstream:  5 to 10 minutes after shock


 Solar wind plasma/IMF
              Bx       By       Bz       Vx       Vy       Vz       N       T
 Upstream     5.448   -3.946   -4.568  -399.958  18.948  -14.969   6.941    99731.6
 Downstream  14.317   -1.766  -16.125  -508.734  37.628 -117.578  17.429   224496.1


 Computed parameters
 dp1   dp2   Xdp   Xb    Xn    vs_rh    vA      cs
 1.864 7.989 4.286 2.661 2.511 604.778  67.317  52.384


 Minimum SMR index within the 2-hour window following shock impact:  -9.60 nT


        nx      ny      nz    thxn    phiyn    thbn      vs       vfms     Ma    Ms
 MC   -0.323  -0.944   0.070 108.831 175.779  78.309   127.332   85.704   0.255 0.200
 MX1  -0.796   0.191  -0.575 142.729 -71.590  72.348   578.268   86.195   3.681 2.874
 MX2  -0.798   0.133  -0.587 142.962 -77.223  74.365   579.175   86.010   3.693 2.890
 MX3  -0.798   0.107  -0.592 142.980 -79.739  75.273   578.920   85.933   3.694 2.894
 VC   -0.722   0.124  -0.681 136.205 -79.682  80.717   551.670   85.556   3.720 2.927
 >>>
```

Listing 2. Example of how to run the Python routine read_shock.py shown in Listing 1 to extract information about a shock event in the list. The example shown in this listing is the event number 142, occurred on 23 June 2000 and observed by ACE (see Figure 1).

TABLE 1　Names of the variables associated with each shock event in the list and shown in Listing 2. The numbers in the first column are the numbers of the fields in the list and shown in the header of the file `full_shock_list_2023.txt`.

1	sn	shock number
2	YY	year
3	MM	month
4	DD	day
5	UTS	UT of shock observation by solar wind monitor
6	UTM	UT of ground magnetic sudden impulse onset
7	nx	x component of shock normal vector
8	ny	y component of shock normal vector
9	nz	z component of shock normal vector
10	thxn	shock impact angle (degrees)
11	phiyn	shock clock angle in the yz plane (degrees)
12	thbn	shock obliquity angle (degrees)
13	vs	shock speed (km/s)
14	cs	sound speed (km/s)
15	vA	Alfvén speed (km/s)
16	vfms	fast magnetosonic speed (km/s)
17	Ma	Alfvénic Mach number
18	Ms	magnetosonic Mach number
19	dp1	upstream solar wind dynamic pressure (nPa)
20	dp2	downstream solar wind dynamic pressure (nPa)
21	Xn	solar wind number density compression ratio;
22	Xdp	solar wind dynamic pressure ratio (dp2/dp1)
23	Xb	magnetic field compression ratio
24	bz1	upstream z component of interplanetary magnetic field (nT)
25	bz2	downstream z component of interplanetary magnetic field (nT)
26	sat	satellite used for calculations: 1 for Wind, 2 for ACE
27	x	x GSE position (in Re) of solar wind monitor at UTS
28	y	y GSE position (in Re) of solar wind monitor at UTS
29	z	z GSE position (in Re) of solar wind monitor at UTS
30	minSMR	minimum SMR within two hours of shock impact

TABLE 2　Upper part: Shock parameters calculated from the shock data base released with this publication. The statistical data are: LPT, lower percentile (20%); median value; mean value; UPT, upper percentile (80%); and standard deviation (STD). There are 603 events in this shock list. Lower part: statistical results of sunspot number observations of the two complete solar cycles (SC) covered in the shock data base: SC23 and SC24.

Shock parameters					
Variable	LPT	Median	Mean	UPT	STD	# Of events
θ_{x_n} [°]	132.96	148.43	147.99	163.56	15.90	603
φ_{y_n} [°]	−105.87	13.10	7.12	120.00	108.41	603
θ_{B_n} [°]	41.05	64.14	59.87	79.77	21.16	603
v_s [km/s]	335.83	435.68	463.20	575.75	161.88	603
M_A	1.74	2.58	3.13	4.05	1.95	603
M_s	1.33	1.86	2.16	2.79	1.18	603
X_N	1.54	1.96	2.13	2.62	0.75	603
X_{dp}	1.45	1.79	1.93	2.36	0.69	603
X_B	1.81	2.49	2.98	3.86	1.56	603

Sunspot numbers (complete solar cycles)					
solar cyle #	LPT	median	mean	UPT	STD	# of events
SC23	13.00	63.00	82.39	150.00	72.74	342
SC24	11.00	44.00	54.08	98.00	47.01	187

The overall statistical properties of sunspot observations and shock parameters are quantified and shown in Table 2. These results, including mean, median, percentile values, and shock number distribution correlation with sunspot numbers, are in excellent agreement with past studies (Kilpua et al., 2015; Oliveira and Raeder, 2015; Oliveira et al., 2018; Rudd et al., 2019).

5 Suggested use of the IP shock data base

The IP shock data base described in this report can be used in many ways. For example, this list can be used in studies involving geomagnetic activity following shock impacts from the geospace to the ground, including particle acceleration by shocks, particle dynamics and energization in the radiation belts, magnetospheric ultra-low frequency (ULF) waves, magnetic field response in geosynchronous orbit, field-aligned currents, role of shocks in substorm triggering, ionospheric irregularities, high-latitude thermosphere response (neutral density and nitric oxide) to shock impacts, ground magnetometer response (dB/dt variations) and subsequent effects on GICs, and many others. Therefore, this shock list can be used in a variety of space physics and space weather investigations.

A major feature of this shock list is the possibility of using the shock impact angle as a factor controlling geomagnetic activity. Oliveira (2023) has recently reviewed the effects of shock impact angles on the subsequent geomagnetic activity and also suggested a few topics for future research.
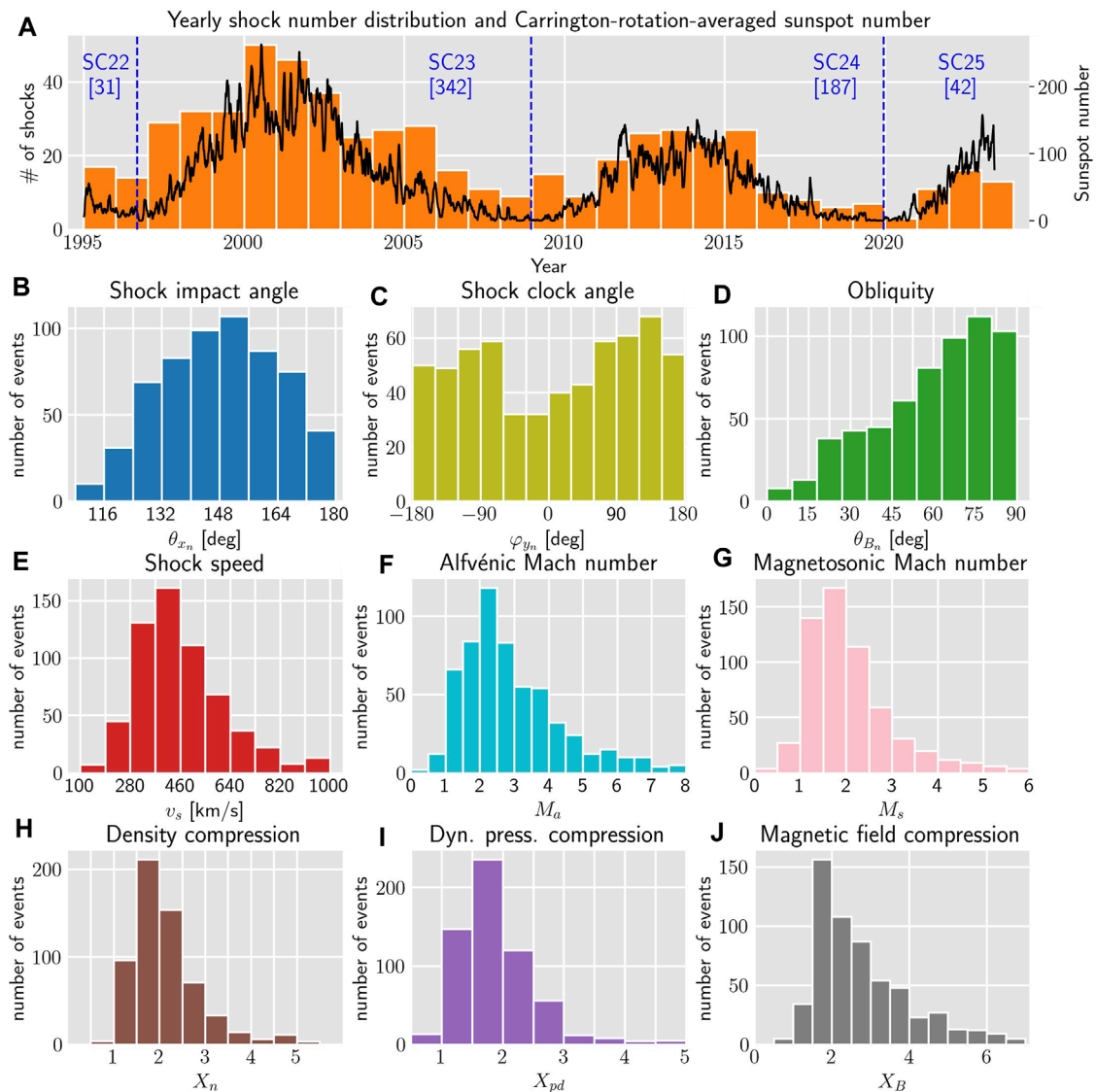
distributions and Carrington-rotation of 25.38 days (Carrington, 1863) averaged sunspot numbers (solid black line). This figure shows a clear correlation between the number of events and sunspot numbers, a result that is already well known (Kilpua et al., 2015; Oliveira and Raeder, 2015; Rudd et al., 2019). Observations show that SC23 was significantly stronger than SC24 based on the overall sunspot numbers, which is reflected on the total number of shocks observed in the corresponding periods (432 and 187, respectively). Zhu et al. (2022) predicted that SC25 will be stronger than SC24 and will reach its maximum value around July 2025. Therefore, according to these predictions, it is reasonable to expect that SC25 will have a similar number of shocks with respect to SC24.

FIGURE 2
Statistical properties of shocks in the data base from January 1995 to May 2023 (603 shocks). Panel **(A)** shock number distribution and Carrington rotation-averaged sunspot numbers. Panels **(B–J)**: number distributions of shock parameters obtained from Eqs 6–17.

1 Shock impact angle effects on intensities and latitudinal extensions of dB/dt variations linked to enhancements of GICs (Carter et al., 2015; Oliveira et al., 2018; Oliveira et al., 2021).

2 Role of shock inclinations in controlling the triggering and wave modes of ULF waves and their interaction with magnetospheric cold plasma and wave-particle interactions (Oliveira et al., 2020; Hartinger et al., 2022).

3 Effects caused by different shock orientations on thermospheric neutral and nitric oxide molecules that control thermosphere heating and cooling affecting the subsequent satellite orbital drag in low-Earth orbit (Oliveira and Zesta, 2019; Zesta and Oliveira, 2019).

4 Shock impact angle effects on the dynamics of radiation belts (e.g., particle acceleration, enhancements, dropouts, and loss of relativistic electrons in the magnetosphere) (Tsurutani et al., 2016; Hajra and Tsurutani, 2018b).

5 Role of shock impact angle in triggering magnetospheric super substorms, with minimum SML < −2,500 nT (Hajra and Tsurutani, 2018a; Tsurutani and Hajra, 2023).

Finally, I would like to urge researchers to perform numerical simulations of shocks with different orientations. For example, Welling et al. (2021) argued that the "most perfect" CME would be very fast and impact Earth head-on. They performed numerical simulations of the impact of a perfect CME on the magnetosphere and concluded that ground dB/dt variations were noted in very low latitude regions because the CME impact was purely frontal. Furthermore, our shock list can be very useful in simulations comparing real observations with results yielded by numerical

simulations of shocks with different orientations for many different space weather purposes.

Data availability statement

The interplanetary shock data base is available at https://zenodo.org/record/7991430. The solar wind plasma data and interplanetary magnetic field data were downloaded from NASA's Coordinated Data Analysis Web (CDAWeb) website (https://cdaweb.gsfc.nasa.gov). SuperMAG geomagnetic index data were downloaded from https://supermag.jhuapl.edu. Daily sunspot number data files were downloaded from the Solar Influences Data Analysis Center of the Royal Observatory of Belgium (https://www.sidc.be/SILSO/datafiles).

Author contributions

The author confirms being the sole contributor of this work and has approved it for publication.

Conflict of interest

The author declares that the research was conducted in the absence of any commercial or financial relationships that could be construed as a potential conflict of interest.

Publisher's note

All claims expressed in this article are solely those of the authors and do not necessarily represent those of their affiliated organizations, or those of the publisher, the editors and the reviewers. Any product that may be evaluated in this article, or claim that may be made by its manufacturer, is not guaranteed or endorsed by the publisher.

References

Abda, Z. M. K., Aziz, N. F. A., Kadir, M. Z. A. A., and Rhazali, Z. A. (2020). A review of geomagnetically induced current effects on electrical power system: principles and theory. *IEEE Access* 8, 200237–200258. doi:10.1109/ACCESS.2020.3034347

Abraham-Shrauner, B. (1972). Determination of magnetohydrodynamic shock normals. *J. Geophys. Res.* 77, 736–739. doi:10.1029/JA077i004p00736

Aguilar-Rodriguez, E., Blanco-Cano, X., Russell, C. T., Jian, L. K., Luhmann, J. G., and Velez, J. C. R. (2010). "Study of interplanetary shocks using multi-spacecraft observations," in *Twelth international solar wind conference, AIP conference proceedings*. Editors M. Maksimovic, K. Issautier, M. Meyer-Vernet, M. Moncuquet, and F. Pantellini (Washington, D.C.: American Institute of Physics), 1216, 467–470. doi:10.1063/1.3395904

Baker, A. B. (2019). *Effect of interplanetary shock impact angle on the occurrence rate and properties of Pc5 waves observed by high-latitude ground magnetometers*. Master's thesis. Blacksburg, Virginia: Virginia Tech.

Balogh, A., Gonzalez-Esparza, J. A., Forsyth, R. J., Burton, M. E., Goldstein, B. E., Smith, E. J., et al. (1995). Interplanetary shock waves: ulysses observations in and out of the ecliptic plane. *Space Sci. Rev.* 72, 171–180. doi:10.1007/BF00768774

Bargatze, L. F., Baker, D. N., McPherron, R. L., and Hones, E. W., Jr. (1985). Magnetospheric impulse response for many levels of geomagnetic activity. *J. Geophys. Res.* 90, 6387–6394. doi:10.1029/JA090iA07p06387

Bhaskar, A., Sibeck, D., Kanekal, S. G., Singer, H. J., Reeves, G., Oliveira, D. M., et al. (2021). Radiation belt response to fast reverse shock at geosynchronous orbit. *Astrophysical J.* 910, 154. doi:10.3847/1538-4357/abd702

Boyd, T. J. M., and Sanderson, J. J. (2003). *The physics of plasmas*. Cambridge, United Kingdom: Cambridge University Press.

Burlaga, L. F. (1971). Hydromagnetic waves and discontinuities in the solar wind. *Space Sci. Rev.* 12, 600–657. doi:10.1007/BF00173345

Cameron, T. G., Jackel, B. J., and Oliveira, D. M. (2019). Using mutual information to determine geoeffectiveness of solar wind phase fronts with different front orientations. *J. Geophys. Res. Space Phys.* 124, 1582–1592. doi:10.1029/2018JA026080

Carrington, R. C. (1863). *Observations of the spots on the Sun, from november 9th 1853 to march 24th 1861 made at redhill*. London, United Kingdom: Williams and Norgate.

Carter, B. A., Yizengaw, E., Pradipta, R., Halford, A. J., Norman, R., and Zhang, K. (2015). Interplanetary shocks and the resulting geomagnetically induced currents at the equator. *Geophys. Res. Lett.* 42, 6554–6559. doi:10.1002/2015GL065060

Clette, F., and Lefèvre, L. (2016). The new sunspot number: assembling all corrections. *Sol. Phys.* 291, 2629–2651. doi:10.1007/s11207-016-1014-y

Colburn, D. S., and Sonett, C. P. (1966). Discontinuities in the solar wind. *Space Sci. Rev.* 5, 439–506. doi:10.1007/BF00240575

Craven, J. D., Frank, L. A., Russell, C. T., Smith, E. E., and Lepping, R. P. (1986). "Global auroral responses to magnetospheric compressions by shocks in the solar wind:

two case studies," in *Solar wind-magnetosphere coupling*. Editors Y. Kamide, and J. A. Slavin (Tokyo, Japan: Terra Scientific), 367–380.

Davis, T. N., and Sugiura, M. (1966). Auroral electrojet activity index AE and its universal time variations. *J. Geophys. Res.* 71, 785–801. doi:10.1029/JZ071i003p00785

Echer, E., de Lucas, A., Hajra, R., de Souza Franco, A. M., Bolzan, M. J. A., and do Nascimento, L. E. S. (2023). Geomagnetic activity following interplanetary shocks in solar cycles 23 and 24. *Braz. J. Phys.* 53, 1–13. doi:10.1007/s13538-023-01294-w

Echer, E., Gonzalez, W. D., Guarnieri, F. L., Dal Lago, A., and Vieira, L. E. A. (2005). Introduction to space weather. *Adv. Space Res.* 35, 855–865. doi:10.1016/j.asr.2005.02.098

Gjerloev, J. W. (2009). A global ground-based magnetometer initiative. *Eos Trans. AGU* 90, 230–231. doi:10.1029/2009EO270002

Goncharov, O., Safrankova, J., Nemecek, Z., Prech, L., Pitna, A., and Zastenker, G. N. (2014). Upstream and downstream wave packets associated with low-Mach number interplanetary shocks. *Geophys. Res. Lett.* 41, 8100–8106. doi:10.1002/2014GL062149

Guo, X.-C., Hu, Y.-Q., and Wang, C. (2005). Earth's magnetosphere impinged by interplanetary shocks of different orientations. *Chin. Phys. Lett.* 22, 3221–3224. doi:10.1088/0256-307X/22/12/067

Hajra, R., and Tsurutani, B. T. (2018a). Interplanetary shocks inducing magnetospheric supersubstorms (SML<-2500 nT): unusual auroral morphologies and energy flow. *Astrophysical J.* 858, 123. doi:10.3847/1538-4357/aabaed

Hajra, R., and Tsurutani, B. T. (2018b). "Magnetospheric "killer" relativistic electron dropouts (REDs) and repopulation: A cyclical process," in *Extreme events in geospace: Origins, predictability and consequences*. Editor N. Buzulukova (Cambridge, MA: Elsevier), 373–400. doi:10.1016/B978-0-12-812700-1.00014-5

Hartinger, M. D., Takahashi, K., Drozdov, A. Y., Shi, X., Usanova, M. E., and Kress, B. (2022). ULF wave modeling, effects, and applications: accomplishments, recent advances, and future. *Front. Astronomy Space Sci.* 9. doi:10.3389/fspas.2022.867394

Jeffrey, A., and Taniuti, T. (1964). *Nonlinear wave propagation*. New York, NY: Academic Press.

Kabin, K. (2001). A note on the compression ratio in MHD shocks. *J. Plasma Phys.* 66, 259–274. doi:10.1017/S0022377801001295

Khazanov, G. V. (2016). *Space weather fundamentals*. Boca Raton, FL: CRC Press.

Kilpua, E. K. J., Lumme, K., Andréeová, E., Isavnin, A., and Koskinen, H. E. J. (2015). Properties and drivers of fast interplanetary shocks near the orbit of the Earth (1995-2013). *J. Geophys. Res. Space Phys.* 120, 4112–4125. doi:10.1002/2015JA021138

Larsen, B. A., Morley, S. K., Niehof, J. T., and Welling, D. T. (2022). *SpacePy*. doi:10.5281/zenodo.3252523

Lepping, R. P., Acuña, M. H., Burlaga, L. F., Farrell, W. M., Slavin, J. A., Schatten, K. H., et al. (1995). The WIND magnetic field investigation. *Space Sci. Rev.* 71, 207–229. doi:10.1007/BF00751330

McComas, D. J., Bame, S. J., Barker, P., Feldman, W. C., Phillips, J. L., Riley, P., et al. (1998). Solar wind electron Proton Alpha monitor (SWEPAM) for the advanced composition explorer. *Space Sci. Rev.* 86, 563–612. doi:10.1023/A:1005040232597

Morley, S. K., Koller, J., Welling, D. T., Larsen, B. A., Henderson, M. G., and Niehof, J. T. (2011). "Spacepy - a Python-based library of tools for the space sciences," in Proceedings of the 9th Python in science Conference (SciPy 2010), Austin, TX, June 28 - July 3, 2010, 67–72.

Newell, P. T., and Gjerloev, J. W. (2012). SuperMAG-based partial ring current indices. *J. Geophys. Res.* 117, 1–15. doi:10.1029/2012JA017586

Newell, P. T., and Gjerloev, J. W. (2011). Evaluation of SuperMAG auroral electrojet indices as indicators of substorms and auroral power. *J. Geophys. Res.* 116. doi:10.1029/2011JA016779

Ogilvie, K. W., Chornay, D. J., Fritzenreiter, R. J., Hunsaker, F., Keller, J., Lobell, J., et al. (1995). SWE, a comprehensive plasma instrument for the WIND spacecraft. *Space Sci. Rev.* 71, 55–77. doi:10.1007/BF00751326

Oh, S. Y., Yi, Y., and Kim, Y. H. (2007). Solar cycle variation of the interplanetary forward shock drivers observed at 1 AU. *Sol. Phys.* 245, 391–410. doi:10.1007/s11207-007-9042-2

Oliveira, D. M., and Samsonov, A. A. (2018). Geoeffectiveness of interplanetary shocks controlled by impact angles: A review. *Adv. Space Res.* 61, 1–44. doi:10.1016/j.asr.2017.10.006

Oliveira, D. M., Arel, D., Raeder, J., Zesta, E., Ngwira, C. M., Carter, B. A., et al. (2018). Geomagnetically induced currents caused by interplanetary shocks with different impact angles and speeds. *Space weather.* 16, 636–647. doi:10.1029/2018SW001880

Oliveira, D. M. (2023). Geoeffectiveness of interplanetary shocks controlled by impact angles: past research, recent advancements, and future work. *Front. Astronomy Space Sci.* 10. doi:10.3389/fspas.2023.1179279

Oliveira, D. M., Hartinger, M. D., Xu, Z., Zesta, E., Pilipenko, V. A., Giles, B. L., et al. (2020). Interplanetary shock impact angles control magnetospheric ULF wave activity: wave amplitude, frequency, and power spectra. *Geophys. Res. Lett.* 47, e2020GL090857. doi:10.1029/2020GL090857

Oliveira, D. M. (2017). Magnetohydrodynamic shocks in the interplanetary space: A theoretical review. *Braz. J. Phys.* 47, 81–95. doi:10.1007/s13538-016-0472-x

Oliveira, D. M., and Ngwira, C. M. (2017). Geomagnetically induced currents: principles. *Braz. J. Phys.* 47, 552–560. doi:10.1007/s13538-017-0523-y

Oliveira, D. M., and Raeder, J. (2014). Impact angle control of interplanetary shock geoeffectiveness. *J. Geophys. Res. Space Phys.* 119, 8188–8201. doi:10.1002/2014JA020275

Oliveira, D. M., and Raeder, J. (2015). Impact angle control of interplanetary shock geoeffectiveness: A statistical study. *J. Geophys. Res. Space Phys.* 120, 4313–4323. doi:10.1002/2015JA021147

Oliveira, D. M., Raeder, J., Tsurutani, B. T., and Gjerloev, J. W. (2016). Effects of interplanetary shock inclinations on nightside auroral power intensity. *Braz. J. Phys.* 46, 97–104. doi:10.1007/s13538-015-0389-9

Oliveira, D. M., Weygand, J. M., Zesta, E., Ngwira, C. M., Hartinger, M. D., Xu, Z., et al. (2021). Impact angle control of local intense dB/dt variations during shock-induced substorms. *Space weather.* 19, e2021SW002933. doi:10.1029/2021SW002933

Oliveira, D. M., and Zesta, E. (2019). Satellite orbital drag during magnetic storms. *Space weather.* 17, 1510–1533. doi:10.1029/2019SW002287

Pizzo, V. J. (1991). The evolution of corotating stream fronts near the ecliptic plane in the inner solar system: 2. Three-Dimensional tilted-dipole fronts. *J. Geophys. Res.* 96, 5405–5420. doi:10.1029/91JA00155

Priest, E. F. (1981). *Solar magnetohydrodynamics*. Dordrecht, Holland: D. Reidel Publishing.

Rostoker, G. (1972). Geomagnetic indices. *Rev. Geophys.* 10, 935–950. doi:10.1029/RG010i004p00935

Rudd, J. T., Oliveira, D. M., Bhaskar, A., and Halford, A. J. (2019). How do interplanetary shock impact angles control the size of the geoeffective magnetosphere? *Adv. Space Res.* 63, 317–326. doi:10.1016/j.asr.2018.09.013

Russell, C. T., Gosling, J. T., Zwickl, R. D., and Smith, E. J. (1983). Multiple spacecraft observations of interplanetary shocks: ISEE three-dimensional plasma measurements. *J. Geophys. Res.* 88, 9941–9947. doi:10.1029/JA088iA12p09941

Russell, C. (2000). The solar wind interaction with the Earth's magnetosphere: A tutorial. *IEEE Trans. Plasma Sci.* 28, 1818–1830. doi:10.1109/27.902211

Samsonov, A. A., Sergeev, V. A., Kuznetsova, M. M., and Sibeck, D. G. (2015). Asymmetric magnetospheric compressions and expansions in response to impact of inclined interplanetary shock. *Geophys. Res. Lett.* 42, 4716–4722. doi:10.1002/2015GL064294

Schwartz, S. J. (1998). "Shock and discontinuity normals, Mach numbers, and related parameters," in *Analysis methods for multi-spacecraft data*. Editors G. Paschmann, and P. W. Daly (Noordwijk, Netherlands: ESA Publications Division), 249–270. no. SR-001 in ISSI Scientific Report.

Selvakumaran, R., Veenadhari, B., Ebihara, Y., Kumar, S., and Prasad, D. S. V. V. D. (2017). The role of interplanetary shock orientation on SC/SI rise time and geoeffectiveness. *Adv. Space Res.* 59, 1425–1434. doi:10.1016/j.asr.2016.12.010

Shi, Y., Oliveira, D. M., Knipp, D. J., Zesta, E., Matsuo, T., and Anderson, B. (2019). Effects of nearly frontal and highly inclined interplanetary shocks on high-latitude field-aligned currents (FACs). *Space weather.* 17, 1659–1673. doi:10.1029/2019SW002367

Smith, A. W., Rae, J., Forsyth, C., Oliveira, D. M., Freeman, P. M., and Jackson, D. (2020). Probabilistic forecasts of storm sudden commencements from interplanetary shocks using machine learning. *Space weather.* 18, e2020SW002603. doi:10.1029/2020SW002603

Smith, C. W., L'Heureux, J., Ness, N. F., Acuña, M. H., Burlaga, L. F., and Scheifele, J. (1998). The ACE magnetic fields experiment. *Space Sci. Rev.* 86, 613–632. doi:10.1023/A:1005092216668

Stone, R. G., and Tsurutani, B. T. (Editors) (1985). "Collisionless shocks in the heliosphere: A tutorial review," *Geophysical monograph series* (Washington, D.C: American Geophysical Union), 34. doi:10.1029/GM034

Takeuchi, T., Russell, C. T., and Araki, T. (2002). Effect of the orientation of interplanetary shock on the geomagnetic sudden commencement. *J. Geophys. Res.* 107, SMP 6-1–SMP 6-10. SMP 6–1–SMP 6–10. doi:10.1029/2002JA009597

Trotta, D., Hietala, H., Horbury, T., Dresing, N., Vainio, R., Wilson, L., III, et al. (2023). Multi-spacecraft observations of shocklets at an interplanetary shock. *Mon. Notices R. Astronomical Soc.* 520, 437–445. doi:10.1093/mnras/stad104

Trotta, D., Vuorinen, L., Hietala, H., Horbury, T., Dresing, N., Gieseler, J., et al. (2022). Single-spacecraft techniques for shock parameters estimation: A systematic approach. *Front. Astronomy Space Sci.* 9. doi:10.3389/fspas.2022.1005672

Tsurutani, B. T., Gonzalez, W. D., Gonzalez, A. L. C., Guarnieri, F. L., Gopalswamy, N., Grande, M., et al. (2006). Corotating solar wind streams and recurrent geomagnetic activity: A review. *J. Geophys. Res.* 111, A07S01–25. doi:10.1029/2005JA011273

Tsurutani, B. T., and Hajra, R. (2023). Energetics of shock-triggered supersubstorms (SML <−2500 nT). *Astrophysical J.* 946, 17. doi:10.3847/1538-4357/acb143

Tsurutani, B. T., Hajra, R., Tanimori, T., Takada, A., Remya, B., Mannucci, A. J., et al. (2016). Heliospheric plasma sheet (HPS) impingement onto the magnetosphere as a cause of relativistic electron dropouts (REDs) via coherent EMIC wave scattering with possible consequences for climate change mechanisms. *J. Geophys. Res. Space Phys.* 121 (10), 156. 130–10. doi:10.1002/2016JA022499

Tsurutani, B. T., Lakhina, G. S., Verkhoglyadova, O. P., Gonzalez, W. D., Echer, E., and Guarnieri, F. L. (2011). A review of interplanetary discontinuities and their geomagnetic effects. *J. Atmos. Solar-Terrestrial Phys.* 73, 5–19. doi:10.1016/j.jastp.2010.04.001

Wang, C., Li, C. X., Huang, Z. H., and Richardson, J. D. (2006). Effect of interplanetary shock strengths and orientations on storm sudden commencement rise times. *Geophys. Res. Lett.* 33 (14). doi:10.1029/2006GL025966

Wang, C., Li, H., Richardson, J. D., and Kan, J. R. (2010). Interplanetary shock characteristics and associated geosynchronous magnetic field variations estimated from sudden impulses observed on the ground. *J. Geophys. Res.* 115. doi:10.1029/2009JA014833

Welling, D. T., Love, J. J., Joshua Rigler, E., Oliveira, D. M., Komar, C. M., and Morley, S. K. (2021). Numerical simulations of the geospace response to a perfect interplanetary coronal mass ejection. *Space weather.* 19, e2020SW002489. doi:10.1029/2020SW002489

Xu, Z., Hartinger, M. D., Oliveira, D. M., Coyle, S., Clauer, C. R., Weimer, D., et al. (2020). Inter-hemispheric asymmetries in the ground magnetic response to interplanetary shocks: the role of shock impact angle. *Space weather.* 18, e2019SW002427. doi:10.1029/2019SW002427

Zesta, E., and Oliveira, D. M. (2019). Thermospheric heating and cooling times during geomagnetic storms, including extreme events. *Geophys. Res. Lett.* 46 (12), 12739–12746. 739–12. doi:10.1029/2019GL085120

Zhu, H., Zhu, W., and He, M. (2022). Solar cycle 25 prediction using an optimized Long short-term memory mode with F10.7. *Sol. Phys.* 297, 157. doi:10.1007/s11207-022-02091-5